Parallel Gate Fidelity of Flip-Flop Qubits in Small 1D- and 2D-Arrays in a Noisy Environment

Marco De Michielis,* Davide Rei, and Elena Ferraro

The long coherence time of donor atom nuclear spin states and of its bounded electron in ^{28}Si can be exploited to define a qubit. This work is focused on a type of donor- and quantum dot-based qubit, the flip-flop (FF) qubit, that leverages antiparallel electron-nuclear spin states of a ^{31}P donor atom controlled by an electric field. It can provide long-range inter-qubit interactions in the order of some hundreds of nanometers, thus relaxing the common constraints and tolerances on inter-qubit distances in donor-based qubits. Simulation results of linear array (LA) and square array (SA) of four FF qubits are presented to study the effect of noise, idle qubits, and simultaneous gating (parallel gating) on gate fidelity. The impact of noise and qubit mutual coupling for both considered types of array are presented and the obtained fidelity results are compared.

1. Introduction

There is a large number of promising semiconductor qubit holders reported in literature[1–4] and the FF qubit has gained interest in the last few years among those based on a synergy of donor atoms and quantum dots in silicon.[5–10]

The FF qubit is constituted by a ^{31}P donor atom embedded in a ^{28}Si bulk and displaced at a distance from the Si/SiO$_2$ interface. A metal gate deposited on top of the SiO$_2$ generates an electric field that controls the position of the donor bounded electron between the donor location and the Si/SiO$_2$ interface.

FF qubits have been proposed and studied for their long range dipole-dipole interactions[5] also because this can relax the common stringent requirements on precise qubit positioning and consequent inter-qubit distances. This opens up the possibility of scaling up the system in one and two dimensions enabling the exploitation of quantum error correction (QEC) codes with higher code-word distances thus with a reduced logical qubit error rate.

In general, a 1D qubit register, due to its almost mono-dimensional spatial distribution, is easier to fabricate than a 2D one and leaves free space along the other in-plane dimension to integrate devices needed for qubit initialization and readout.[11] However, the expected qubit density in 1D lattices is limited by the maximum array length achievable. This limit can be partially overcome by interconnecting different 1D qubit arrays with T-sections as proposed in ref. [12] for a different qubit type.

There are different QEC codes that can be implemented on a 1D array of qubits but the common need of SWAP chains to move qubit states between distant qubits in a linear-nearest-neighbor qubit array impacts all the qubits, negatively affecting the system fault-tolerance.[13] Using segmented 1D arrays of qubits can ease achieving a fault-tolerant system.[14]

On the other hand, 2D qubit registers could reach an higher qubit density than 1D ones, opening up the creation of logical qubits based on a larger number of physical ones. However, high qubit spatial densities entails tight spatial constraints on the positioning of qubit initialization/readout devices and routing of metal gates for control signals. Sparse 2D array solutions can be employed to mitigate this issue but at the expense of a qubit density reduction.[15]

Most importantly, 2D qubit arrays are open to the implementation of topological quantum error correction codes[16] where the surface codes[17] are currently the most promising candidates for a large-scale fault-tolerant quantum computer due to their high error threshold. The surface code implementation prescribes the simultaneous application of CNOT operations for both X and Z stabilizers on the whole 2D array. A reliable assessment of the gate fidelity reduction induced by the parallel gating needs to be accounted for a correct estimation of the surface code error.

Noise effects on FF qubits simultaneously operated and displaced in a LA have already been simulated in ref. [7] but there are no references in literature on 1D and 2D arrays of noisy and mutually disturbed FF qubits, so this motivate the present simulation study.

M. De Michielis, D. Rei, E. Ferraro
CNR-IMM
Unit of Agrate Brianza
Via C. Olivetti 2, Agrate Brianza, MB 20864, Italy
E-mail: marco.demichielis@cnr.it

The ORCID identification number(s) for the author(s) of this article can be found under https://doi.org/10.1002/qute.202300455

2. Results

We simulated two types of arrays made up of four FF qubits, one with qubits displaced in a linear way and the other one in a square lattice. The qubits are noisy and they mutually disturb each other.
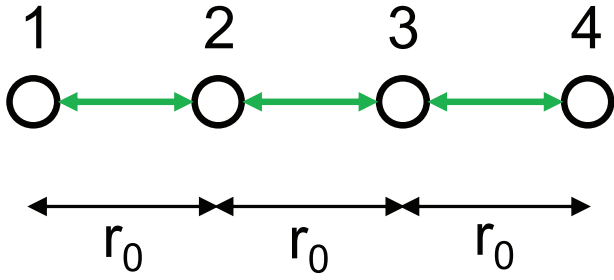
ADVANCED
SCIENCE NEWS

www.advancedsciencenews.com

ADVANCED
QUANTUM
TECHNOLOGIES

www.advquantumtech.com

Figure 1. Scheme of the LAcomposed by four FFqubits equally displaced, where r_0 is the inter-qubit distance. Only the first neighbour inter-qubit interactions are included in the model and they are sketched in green.

We took into account the charge noise by modeling it as 1/f noise with an amplitude $\alpha_{\Delta E_z}$ as specified in the Experimental Section. Noises are considered not correlated between qubits thus each qubit in the array is affected by a different noise instance. As a figure of merit to compare the different cases, we used the entanglement fidelity F, or equally the entanglement infidelity $1 - F$ (see Experimental Section).

2.1. Linear Array

In a LA the qubits are displaced on a regular linear lattice with an inter-qubit distance r_0 as shown in **Figure 1**.

In this study r_0 is set to 360 nm and for this type of array only the first neighbour inter-qubit interactions are included in the model.

The Hamiltonian $\hat{H}^{LA}$ describing a LA of four FF qubits is:

$$\hat{H}^{LA} = \sum_{i=1}^{4} \hat{H}^i + \sum_{i=1}^{3} \hat{H}_{int}^{i,i+1} \tag{1}$$

where the Hamiltonian $\hat{H}^i$ of the single FF qubit is:

$$\hat{H}^i = \hat{H}_{B_0} + \hat{H}_A + \hat{H}_{Orb} \tag{2}$$

where

$$\hat{H}_{B_0} = \gamma_e B_0 \left[\hat{\mathbb{1}} + \left(\frac{\hat{\mathbb{1}}}{2} + \frac{d\,e\Delta E_z}{2h\epsilon_0}\hat{\sigma}_z + \frac{V_t}{2\epsilon_0}\hat{\sigma}_x \right) \Delta_\gamma \right] \hat{S}_z - \gamma_n B_0 \hat{I}_z \tag{3}$$

$$\hat{H}_A = A\left(\frac{\hat{\mathbb{1}}}{2} - \frac{d\,e\Delta E_z}{2h\epsilon_0}\hat{\sigma}_z - \frac{V_t}{2\epsilon_0}\hat{\sigma}_x \right) \mathbf{S} \cdot \mathbf{I} \tag{4}$$

describe the Zeeman splitting caused by a constant magnetic field B_0 (Equation (3)) and the hyperfine interaction (Equation (4)), respectively. In particular, in Equation (3), Δ_γ takes into account the variation of the electron gyromagnetic ratio γ_e (27.97 GHzT^{-1}) between the nucleus and the interface, while $\gamma_n = 17.23$ MHzT^{-1} is the constant nuclear gyromagnetic ratio. $\mathbf{S}$ ($\mathbf{I}$) are the electron (nuclear) spin operators with $\hat{z}$ component S_z (I_z) and $B_0 = 0.4$ T. Moreover, V_t is the tunnel coupling between the donor and the interface potential wells, $\Delta E_z = E_z - E_z^0$ where E_z^0 is the vertical electric field at the ionization point, i.e., the point in which the electron is shared halfway between the donor and
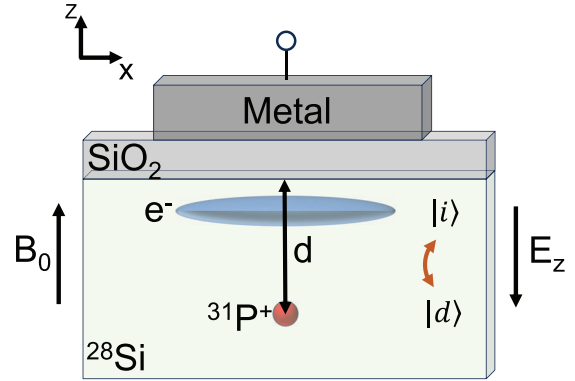
a)
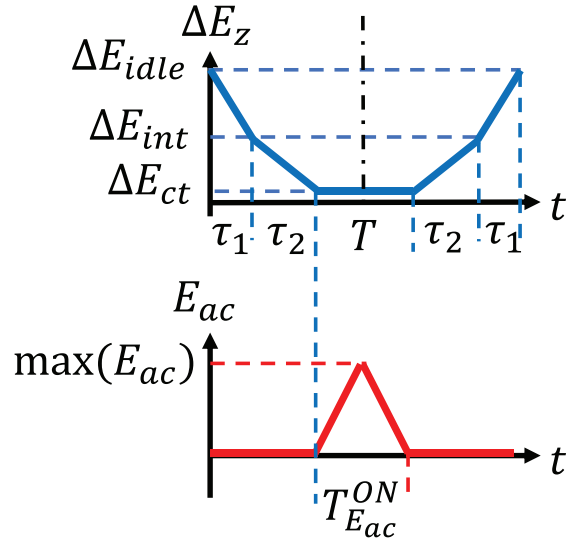
b)

Figure 2. a) FF qubit scheme where a ^{31}P donor atom is embedded in a ^{28}Si bulk, positioned at a distance d from a Si/SiO$_2$ interface and under the application of a constant magnetic field B_0. An electric field E_z, generated along the $\hat{z}$-axis by an external gate voltage applied to the metal gate on the top, controls the system states by moving the electron position between the nucleus (state $|d\rangle$) and the quantum dot at the interface (state $|i\rangle$). b) Waveforms of the control signals applied to the metal gate to generate the single-qubit gates $R_z(-\frac{\pi}{2})$, $R_x(-\frac{\pi}{2})$ and the two-qubit $\sqrt{iSWAP}$ gate. The R_z gate requires the application of an electric dc signal (in blue). R_x operations requires the simultaneous application to the qubit under manipulation of both the dc signal and the ac one (where its envelope signal is reported in red), the last one being in resonance with the FF qubit energy. In this way R_x is performed by means of an Electric Dipole Spin Resonance (EDSR) method. Regarding the $\sqrt{iSWAP}$ gate, the same dc signal has to be applied to both qubits (1 and 2) under manipulation. After that, a rephasing gate $R_z(\theta)$ has to be applied to qubit 1 to complete the operation as reported in the last line of Table 1.

the interface, $\epsilon_0 = \sqrt{V_t^2 + (de\Delta E_z/h)^2}$ is the energy difference between the orbital eigenstates, where h is the Planck's constant, d is the distance from the interface, hereafter $d = 15$ nm, and e is the elementary charge.

In Equation (4), the hyperfine coupling A is a function of the vertical electric field E_z applied by the gate and, in order to obtain its functional form, the results reported in ref. [5] are fitted

ADVANCED
SCIENCE NEWS
www.advancedsciencenews.com

ADVANCED
QUANTUM
TECHNOLOGIES
www.advquantumtech.com

Table 1. Parameters and values of the control sequences to generate $R_z(-\frac{\pi}{2})$, $R_x(-\frac{\pi}{2})$ and $\sqrt{iSWAP}$ gates. All the presented gates have the same adiabatic factor K, defined as in ref. [8], and set to $K = 19$.

Operation	V_t [GHz]	ΔE_{idle} [kV m^{-1}]	ΔE_{int} [kV m^{-1}]	ΔE_{ct} [kV m^{-1}]	τ_1 [ns]	τ_2 [ns]	T [ns]	$T^{ON}_{E_{ac}}$ [ns]	max($E_{ac}(t)$) [kV m^{-1}]
$R_z(-\frac{\pi}{2})$	11.29	10	1.3	0.290	2	16	0.08	–	–
$R_x(-\frac{\pi}{2})$	14.00	10	4.3	0	0.2	0.5	94.5	90	0.5492
$\sqrt{iSWAP}$	11.30	10	1.3	0	2	20	200	–	–
$(R_z(\theta)_{q_1})$	11.30	10	1.3	0	2	20	9.8	–	–

with the function $A_0 / \left(1 + \exp\left(c\Delta E_z\right)\right)$, where $A_0 = 117$ MHz is the bulk value of A, obtaining the fit parameter $c = 5.174 \cdot 10^{-4}$ mV^{-1}.[8]

The orbital part $\hat{H}_{Orb}$, which gives a treatment of the electron position between the interface and the donor as a two level system allowing a full quantum mechanical description of the system, is given by

$$\hat{H}_{Orb} = -\frac{\epsilon_0}{2}\hat{\sigma}_z - \frac{d\,eE_{ac}(t)\cos(\omega_E t + \phi)}{2h}\left(\frac{d\,e\Delta E_z}{h\epsilon_0}\hat{\sigma}_z + \frac{V_t}{\epsilon_0}\hat{\sigma}_x\right) \quad (5)$$

where $E_{ac}(t)$ is the time dependent amplitude of an oscillating electric field with pulsation ω_E and phase ϕ.

In Equation (1), H^{ij}_{int} is the interaction Hamiltonian between qubits i and j defined as:

$$\hat{H}^{ij}_{int} = \frac{1}{4\pi\varphi_0\varphi_r r^3}\left[\mathbf{p}_i \cdot \mathbf{p}_j - \frac{3(\mathbf{p}_i \cdot \mathbf{r})(\mathbf{p}_j \cdot \mathbf{r})}{r^2}\right] \quad (6)$$

where φ_0 is the vacuum permittivity, φ_r is the material dielectric constant (equals to 11.7 for silicon), $\mathbf{r}$ is the vector distance between the two qubits and $\mathbf{p}_{i(j)} = \frac{ed}{2}\left(\hat{\mathbb{1}}_{i(j)} + \hat{\sigma}^{id}_{z,i(j)}\right)$ is the dipole operator of the qubit to whom is associated the position operator

$$\hat{\sigma}^{id}_z = \frac{d\,e\Delta E_z}{h\epsilon_0}\hat{\sigma}_z + \frac{V_t}{\epsilon_0}\hat{\sigma}_x \quad (7)$$

whose eigenstates $|i\rangle$ and $|d\rangle$, see **Figure 2a**, indicate if the electron is localized near the interface or the donor, respectively and

$$\hat{\sigma}_z = |g\rangle\langle g| - |e\rangle\langle e| \quad (8)$$

$$\hat{\sigma}_x = |g\rangle\langle e| + |e\rangle\langle g| \quad (9)$$

are the Pauli matrices and $|g\rangle$ ($|e\rangle$) is the electron ground (excited) state.

The quantum gates included in this study, namely $R_z(-\frac{\pi}{2})$, $R_x(-\frac{\pi}{2})$ and $\sqrt{iSWAP}$, constitute a universal set of quantum gates with control sequences of $\Delta E_z(t)$ and $E_{ac}(t)$ signals derived as done in ref. [8]. The typical signal waveforms to generate those gates are reported in Figure 2b and the corresponding parameters are reported in **Table 1**.

The noise is included by adding a time variable signal to the ideal gate control one as specified in the Experimental Section. These noisy quantum gates are applied to one, two or four qubits depending on the type of operation, that is a one- or a two-qubit

gate, and on the particular effect to investigate, namely idling qubits effect on a single gate or parallel gating implications for two simultaneous gates. Therefore different configurations of manipulated qubits are achievable in a LA of four FF qubits as reported in **Table 2**.

2.1.1. Effects of Idle Qubits

We present simulation results useful to investigate the effects of idling qubits on the gate infidelity. **Figure 3a,b** illustrate the infidelity $1 - F$ versus the noise amplitude $\alpha_{\Delta E_z}$ when a single qubit gate $R_z(-\frac{\pi}{2})$ and $R_x(-\frac{\pi}{2})$, respectively, is applied to one qubit while the other ones are idling, namely for c1 and c2 configurations. The infidelity for $R_z(-\frac{\pi}{2})$ in the best configuration, that corresponds to c1 in which the operated qubit is disturbed by only one idle qubit, assumes values from $6.6 \cdot 10^{-5}$ (F = 99.993%) to $1.3 \cdot 10^{-4}$ (F = 99.987%) when noise goes from 0 to 100 Vm^{-1}, while the $R_x(-\frac{\pi}{2})$ gate in the same configuration gives higher results ranging from $5.8 \cdot 10^{-4}$ (F = 99.94%) to $1.6 \cdot 10^{-3}$ (F = 99.84%).

Figure 3c shows the same for $\sqrt{iSWAP}$ gates operated on two qubits while the other two are idling (c12 and c23 configurations).

Moreover in the figure we added the simulated infidelities of new $\sqrt{iSWAP}$ gates, named configuration-optimized gates, that are gates obtained with control sequences manually searched to minimize the infidelity by taking into account the idling qubit effects. The configuration-optimized sequences for $\sqrt{iSWAP}$ gates on a LA for configurations c12 and c23 are reported in **Table 3**.

Table 2. Correspondence between configurations and operations in the LA. Configurations in brackets are equivalent to the main one due to geometric symmetries of the array. c1 and c2, apply for one-qubit operations whereas c12, c13, c14, and c23 apply for two simultaneous one-qubit gates. c12 and c23 configurations are considered for single two-qubit gates and c12-34 configuration is assumed only for two simultaneous two-qubit gates.

Configuration	Operation(s)
c1 (c4)	$Op. \otimes \mathbb{1} \otimes \mathbb{1} \otimes \mathbb{1}$
c2 (c3)	$\mathbb{1} \otimes Op. \otimes \mathbb{1} \otimes \mathbb{1}$
c12 (c34)	$Op. \otimes Op. \otimes \mathbb{1} \otimes \mathbb{1}$
c13 (c24)	$Op. \otimes \mathbb{1} \otimes Op. \otimes \mathbb{1}$
c14	$Op. \otimes \mathbb{1} \otimes \mathbb{1} \otimes Op.$
c23	$\mathbb{1} \otimes Op. \otimes Op. \otimes \mathbb{1}$
c12-34	$Op. \otimes Op. \otimes Op. \otimes Op.$

**ADVANCED
SCIENCE NEWS**

www.advancedsciencenews.com

**ADVANCED
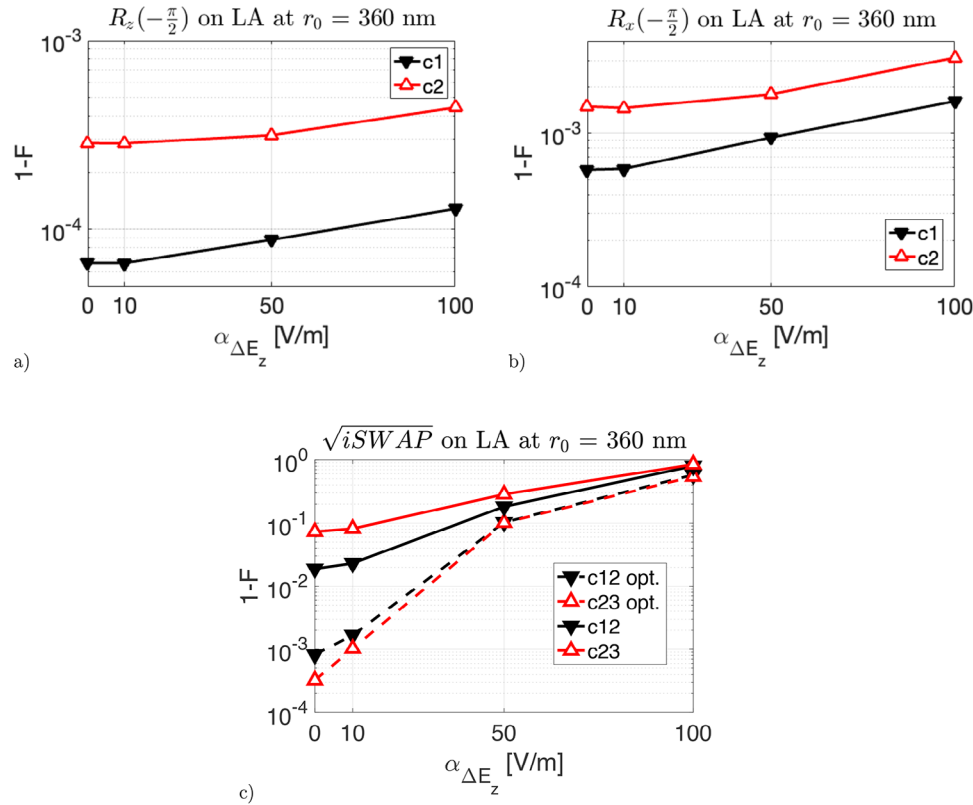QUANTUM
TECHNOLOGIES**

www.advquantumtech.com

Figure 3. a) $R_z(-\frac{\pi}{2})$ infidelity versus noise amplitude $\alpha_{\Delta E_z}$. The quantum gate is disturbed by noise and by idle qubits, where c1 and c2 represent the two configurations considered. b) Same as case a) but for the $R_x(-\frac{\pi}{2})$ gate. c) $\sqrt{iSWAP}$ infidelity comparison for both c12 and c23 configurations between standard (solid lines) and configuration-optimized sequences (dashed lines).

The optimized sequences provide a gain of around two orders of magnitudes in the infidelity that for the c23 configuration in the zero noise case gives a value of $3.2 \cdot 10^{-4}$ (F = 99.97%).

2.1.2. Effects of Simultaneous Gating

In order to perform many operations during a gate time, simultaneous gating is considered and it reasonably produces an overall increased gate infidelity with respect to the not simultaneous case. **Figure** 4a shows, on the left, the 1-F as a function of $\alpha_{\Delta E_z}$ for the different configurations (c12, c13, c14, and c23) of the $R_z(-\frac{\pi}{2})$ gate. On the right side of the figure, we reported how the infidelity is reduced when the active inter-qubit distance r is increased to r_0, $2r_0$, and $3r_0$ and the noise is switched off.

Table 3. Parameters and values of the sequences for optimized LA c12 and LA c23 $\sqrt{iSWAP}$ gates. All the remaining parameters maintain the same values reported in Table 1.

Operation	T [ns]
$\sqrt{iSWAP}$ c12	204
$(R_z(\theta)_{q_1})$	4
$\sqrt{iSWAP}$ c23	205.5
$(R_z(\theta)_{q_2})$	0.1

As it can be seen, the different configurations c_{ij} have different $r = (j - i)r_0$. The c14 configuration gives the better infidelity values: $2.6 \cdot 10^{-4}$ (F = 99.97%) in the zero noise case and $5.1 \cdot 10^{-4}$ (F = 99.95%) in correspondence to $\alpha_{\Delta E_z} = 100\,\mathrm{Vm}^{-1}$. The same study is repeated for the $R_x(-\frac{\pi}{2})$ gate in Figure 4b with infidelity values from $1.5 \cdot 10^{-3}$ (F = 99.85%) for the zero noise case to $4 \cdot 10^{-3}$ (F = 99.60%) for the higher noise case in the c14 configuration. In Figure 4c, the gate infidelity as a function of noise amplitude is presented for two simultaneous c12-optimized $\sqrt{iSWAP}$ gates. In this case the infidelity is more affected by the parallel gating and in the zero noise case gives a value of $1.2 \cdot 10^{-2}$ (F = 98.84%).

2.2. Square Array

In a SA the four qubits are displaced on a bi-dimensional lattice with a step r_0 as shown in **Figure** 5. Differently from the LA case, all the inter-qubit interactions are included in the model for a SA case. The Hamiltonian describing a SA of four FF qubits is:

$$\hat{H}^{SA} = \sum_{i=1}^{4} \hat{H}^i + \sum_{i=1}^{3} \sum_{j=i+1}^{4} \hat{H}_{int}^{i,j} \tag{10}$$

where $\hat{H}^i$ and $\hat{H}_{int}^{ij}$ are defined in Equations (1) and (6), respectively. The configurations studied in the SA are fewer than those

ADVANCED
SCIENCE NEWS
www.advancedsciencenews.com

ADVANCED
QUANTUM
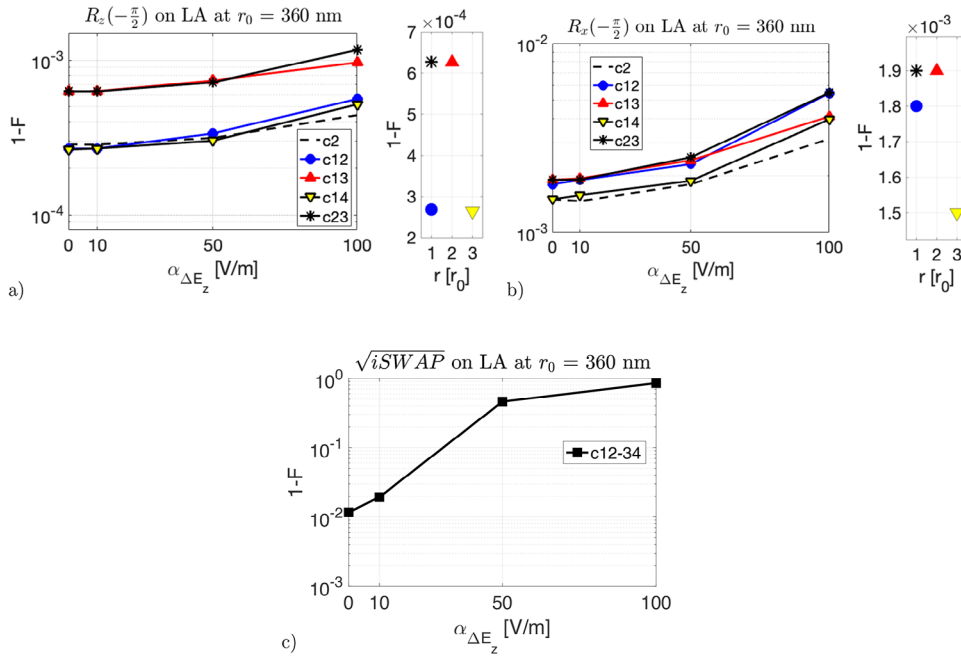**TECHNOLOGIES**
www.advquantumtech.com

Figure 4. a) Two simultaneous $R_z(-\frac{\pi}{2})$ infidelity versus noise amplitude (left) for c12, c13, c14, and c23 configurations. c2 is shown only for comparison with the one-qubit gate. The effect of the distance r between the manipulated qubits on the infidelity is also presented (right) when noise is switched off. b) Same as the previous panel but for the $R_x(-\frac{\pi}{2})$ gate. c) Two simultaneous c12-optimized $\sqrt{iSWAP}$ infidelity versus noise amplitude in a LA.

of the LA, as clearly shown in **Table 4**, due to the enhanced geometric symmetries of the SA with respect the LA.
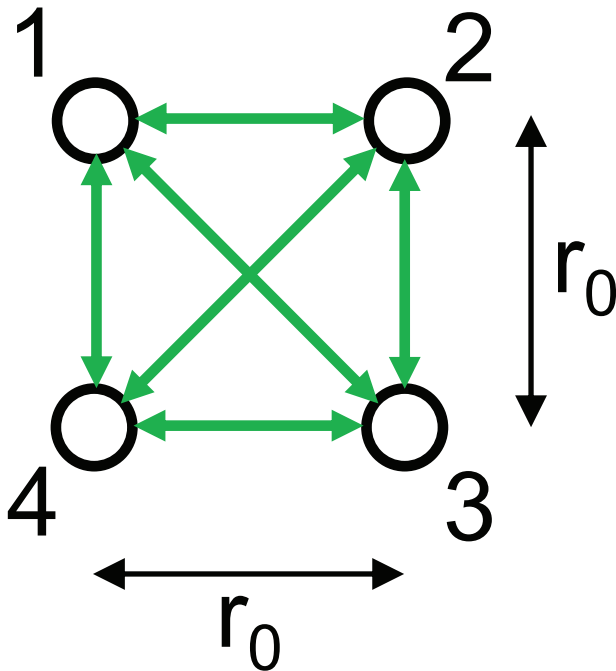

Figure 5. Scheme of four qubits displaced in an equally spaced SA with a lattice step r_0. All the inter-qubit dipole–dipole interactions are included in the array model and highlighted in green.

2.2.1. Effects of Idle Qubits

The simulation results useful to investigate the effects of idling qubits in a SA on the gate infidelity are hereafter reported. **Figure 6a,b** illustrate how the infidelity is affected by noise when one-qubit gates are operated whereas Figure 6c shows the same when a standard and optimized $\sqrt{iSWAP}$, with sequence presented in **Table 5**, are applied to qubits one and two while the remaining ones are idling.

The configuration c1 presented, due to the higher symmetry of the SA with respect to the LA, is exactly equivalent to all the other possible configurations when the idle qubits effect is included. From a quantitative point of view the obtained infidelity goes from $4.1 \cdot 10^{-4}$ (F = 99.96%) to $6.3 \cdot 10^{-4}$ (F = 99.94%) for $R_z(-\frac{\pi}{2})$ and from $2.1 \cdot 10^{-3}$ (F = 99.79%) to $4.1 \cdot 10^{-3}$ (F = 99.59%) for $R_x(-\frac{\pi}{2})$. The infidelity for the $\sqrt{iSWAP}$ in the zero noise case is $4.2 \cdot 10^{-4}$ (F = 99.96%).

Table 4. Correspondence between configurations and operations in the SA of four qubits. c1 applies for one-qubit operations whereas c12 and c13 arises for two simultaneous one-qubit gates. Only c12 is considered for a single $\sqrt{iSWAP}$ and c12-34 is assumed for two simultaneous $\sqrt{iSWAP}$.

Configuration	Operation(s)
c1 (c2,c3,c4)	$Op. \otimes \mathbb{I} \otimes \mathbb{I} \otimes \mathbb{I}$
c12 (c34,c14,23)	$Op. \otimes Op. \otimes \mathbb{I} \otimes \mathbb{I}$
c13 (c24)	$Op. \otimes \mathbb{I} \otimes Op. \otimes \mathbb{I}$
c12-34	$Op. \otimes Op. \otimes Op. \otimes Op.$

**ADVANCED
SCIENCE NEWS**

www.advancedsciencenews.com

**ADVANCED
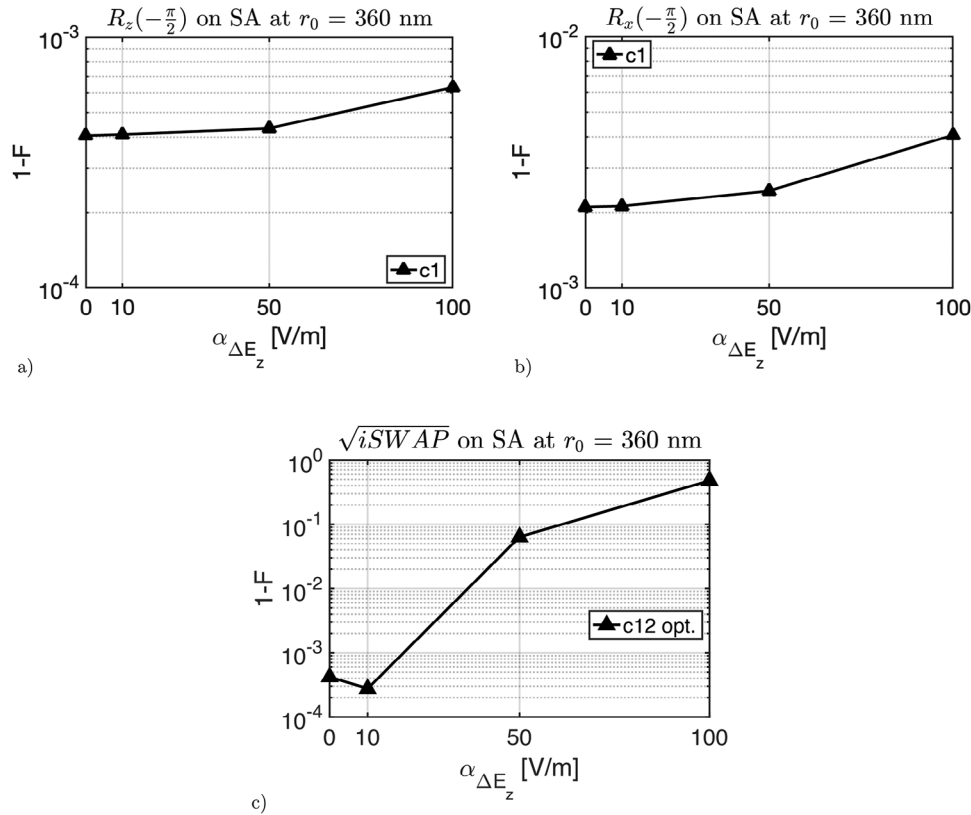QUANTUM
TECHNOLOGIES**

www.advquantumtech.com

Figure 6. a) $R_z(-\frac{\pi}{2})$ infidelity versus noise amplitude with the gate disturbed also by idling qubits. b) Same as case a) but for the $R_x(-\frac{\pi}{2})$ gate. c) Infidelity of an optimized $\sqrt{iSWAP}$ gate as a function of $\alpha_{\Delta E_z}$ and affected by idle qubits. The counter-intuitive initial fidelity decrease can be due to the statistical error of 100 run noises.

2.2.2. Effects of Simultaneous Gating

Similarly to what done for the LA case, simultaneous gating effects on the gate infidelity are presented in **Figure 7a,b** for the SA configuration c12 and c13 of one-qubit gates. In both cases the c12 configuration gives the better infidelity values ranging from $9.3 \cdot 10^{-4}$ (F = 99.91%) to $1.6 \cdot 10^{-3}$ (F = 99.84%) for $R_z(-\frac{\pi}{2})$ and from $2.7 \cdot 10^{-3}$ (F = 99.73%) to $5.4 \cdot 10^{-3}$ (F = 99.46%) for $R_x(-\frac{\pi}{2})$.

Figure 7c reports the simulation results for the two $\sqrt{iSWAP}$ gates showing an infidelity in the zero noise case of $2.2 \cdot 10^{-2}$ (F = 97.81%).

2.3. Comparison Between Infidelities in LA and SA

We collect the infidelity results from both the LA and SA sets, when no noise is present, to compared them in **Figure 8**.

Table 5. Parameters and values of the sequence for a SA c12-optimized $\sqrt{iSWAP}$. All the other parameters assume values reported in Table 1.

Operation	T [ns]
$\sqrt{iSWAP}$ c12	203
$(R_z(\theta)_{q_1})$	0.1

Figure 8a focus on the LA-SA infidelity comparisons of three different configurations for the $R_z(-\frac{\pi}{2})$ gate: a configuration representative of the idling qubit effects (c1); and the best and worst configurations, namely the configurations allowing for lower and higher infidelities, respectively, when parallel gating arises. A similar comparison is provided for the $R_x(-\frac{\pi}{2})$ gate in Figure 8b. For the same purpose Figure 8c shows a LA-SA infidelity comparison for the c12 and c12–34 configurations.

3. Discussion

First of all, we discuss infidelity results on LA. When investigating the effect of idle qubits for one-qubit operations, Figure 3a,b show that c2 infidelity is always higher than c1. This is because the qubit under manipulation in c2 is affected by two nearest neighbor idle qubits, while only one nearest neighbor qubit disturbs the active one in c1. Specifically, c1 includes a qubit positioned on the first edge of the LA. In correspondence to $\alpha_{\Delta E_z} = 50$ Vm^{-1}, that is a realistic noise amplitude for the FF qubits, the infidelity is equal to $8.8 \cdot 10^{-5}$ (F = 99.991%) for $R_z(-\frac{\pi}{2})$ and $9.4 \cdot 10^{-4}$ (F = 99.91%) for $R_x(-\frac{\pi}{2})$. For a two-qubit operation, namely the $\sqrt{iSWAP}$ gate, Figure 3c highlights that a $\sqrt{iSWAP}$ on c23 has a higher infidelity compared to c12. This is due to each qubit under manipulation being disturbed by one nearest neighbor idling qubit. In contrast, c12 has a qubit located on one edge of the
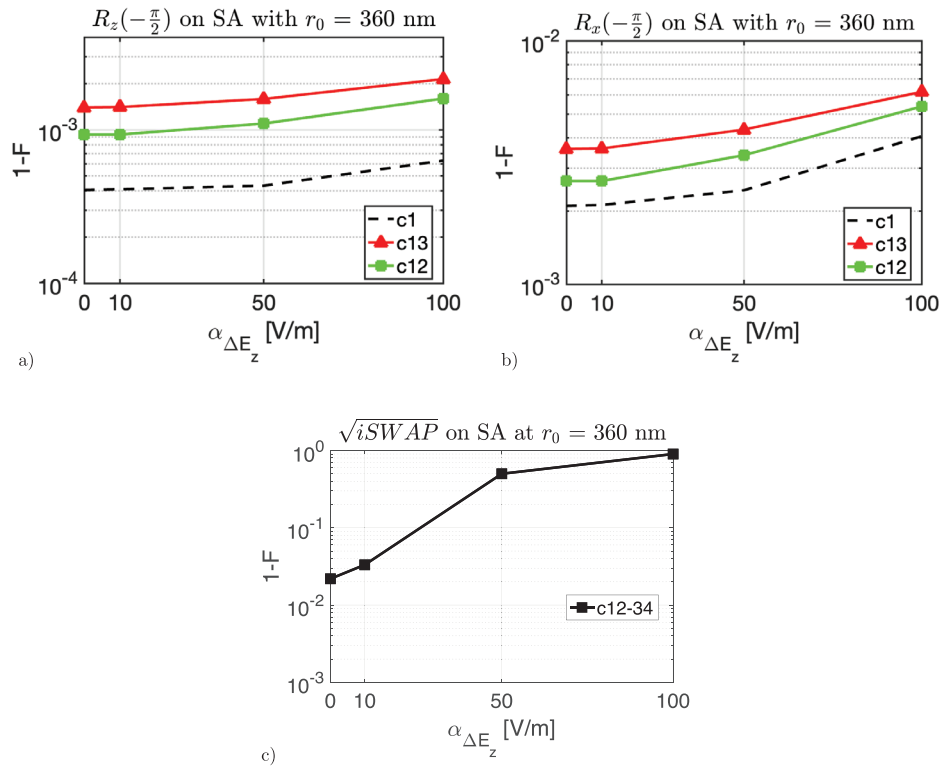
**ADVANCED
SCIENCE NEWS**

www.advancedsciencenews.com

**ADVANCED
QUANTUM
TECHNOLOGIES**

www.advquantumtech.com

Figure 7. a) Two simultaneous $R_z(-\frac{\pi}{2})$ infidelity versus noise amplitude for c12 and c13 configurations. c1 is shown for comparison. b) Same as above but for the $R_x(-\frac{\pi}{2})$ gate. c) Two simultaneous c12-optimized $\sqrt{iSWAP}$ infidelity versus noise amplitude.

LA. To achieve a 99% fidelity at low noise values, configuration-optimized $\sqrt{iSWAP}$ gate sequences are required, even if its F is strongly deteriorated to 90 % when $\alpha_{\Delta E_z} = 50$ Vm^{-1}. Considering the effects of parallel gating, the right panels of Figure 4a,b point out that c14 has a gate infidelity closer to c2. This is because the active FF qubits in c14 are displaced by r = $3r_0$, and only two idling FF qubits affect the active ones. Both qubits in c14 are positioned on the edges of the LA. Focusing on the case in correspondence to $\alpha_{\Delta E_z} = 50$ Vm^{-1}, the infidelities reported are equal to $3 \cdot 10^{-4}$ (F = 99.97%) for $R_z(-\frac{\pi}{2})$ and $1.9 \cdot 10^{-3}$ (F = 99.81%) for $R_x(-\frac{\pi}{2})$. On the other hand, c23 is the worst configuration as the operated qubits are closer (r = r_0) and disturbed by two idling ones, without any edge qubits present. Figure 4c indicates that a high infidelity of parallel $\sqrt{iSWAP}$ (c12-34) is inevitably present even for low level of noise.

After discussing the results on a LA of four FF qubits, we shift our focus on the SA results. Regarding the gate fidelity degradation induced by idling qubits, Figure 6a,b simply illustrate that $1 - F(R_z(-\frac{\pi}{2})) < 1 - F(R_x(-\frac{\pi}{2}))$ corresponding to infidelities respectively equal to $4.3 \cdot 10^{-4}$ (F = 99.96%) and $2.4 \cdot 10^{-3}$ (F = 99.76%), while Figure 6c emphasizes the importance of configuration-optimized sequences in restoring acceptable gate fidelities at least for low noise levels. At the selected noise value of $\alpha_{\Delta E_z} = 50$ V/m the infidelity of $\sqrt{iSWAP}$ is deteriorated to 0.06 (F = 94 %). For the one-qubit operations depicted in Figure 7a,b, parallel gating yields $1 - F(c13) > 1 - F(c12)$ due to enhanced inter-qubit coupling primarily caused by idle qubits rather than gated

ones. Specifically, each qubit under manipulation in c13 exhibits strong coupling with two idle qubits, whereas each gated qubit in c12 is mainly affected by one idle qubit. The infidelities obtained in this case in correspondence to the best configuration and to $\alpha_{\Delta E_z} = 50$ Vm^{-1} are $1.1 \cdot 10^{-3}$ (F = 99.89%) for $R_z(-\frac{\pi}{2})$ and $3.4 \cdot 10^{-3}$ (F = 99.66%) for $R_x(-\frac{\pi}{2})$. Notably, Figure 7c demonstrates a high infidelity of parallel $\sqrt{iSWAP}$ (c12-34) even at low noise levels. A comparison of the infidelity results obtained in LA and SA, as shown in Figure 8, reveals that SA exhibits higher infidelity than LA for both the effects of idle qubits and parallel gating in almost all considered configurations (except for c12, which are similar in Figure 8c). This overall trend stems from a higher qubit packing in SA compared to LA, leading to increased inter-qubit couplings.

The simulation results show that the infidelities obtained by applying simultaneously gates, in particular the $\sqrt{iSWAP}$ ones, to the four FF qubits affected by a reasonable noise level (50 Vm^{-1}) are not sufficiently small to successfully implement the Surface Code. In fact, the infidelities of the reported $\sqrt{iSWAP}$ gates result in an average gate error exceeding 1%, a value that represents the error threshold for a fault-tolerant implementation of the Surface Code.[17] A strategy to mitigate the effects of a full simultaneous gating could be to apply a partial time serialization, alternating one gate from the Z- and then one gate from the X-stabilizer circuit in order to increase the distance between the qubits simultaneously manipulated but at the cost of a doubling of each stabilizer execution time. However full simul-
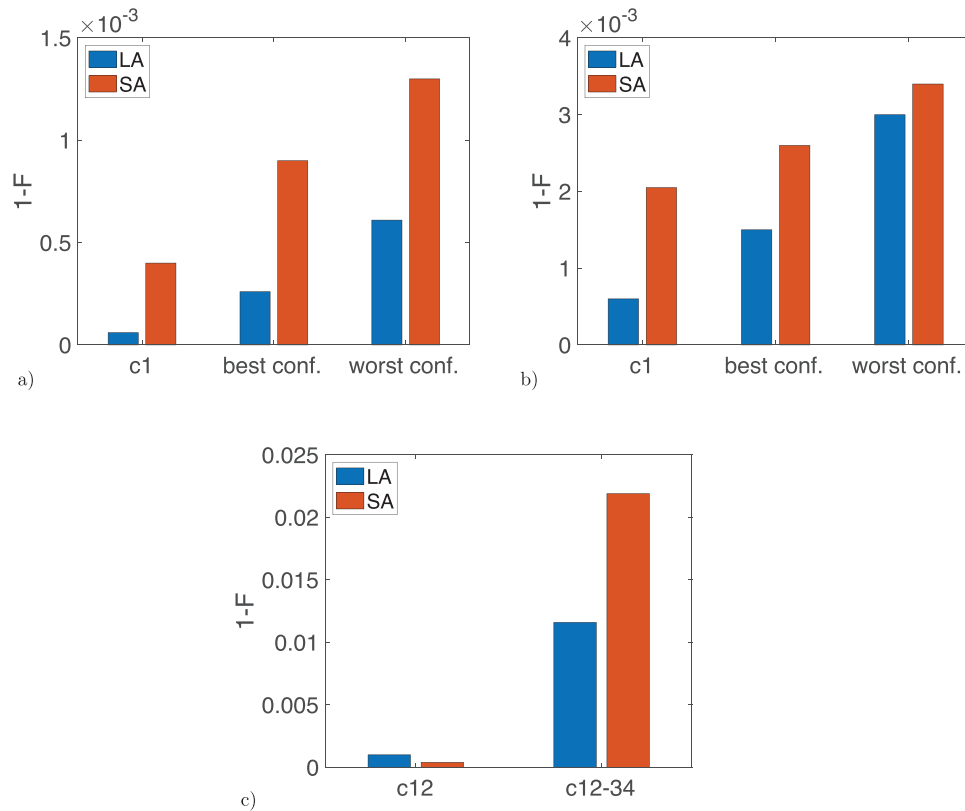
**ADVANCED
SCIENCE NEWS**

www.advancedsciencenews.com

**ADVANCED
QUANTUM
TECHNOLOGIES**

www.advquantumtech.com

Figure 8. Comparison between gate infidelities in LA and SA without noise. a) Infidelities of $R_z(-\frac{\pi}{2})$ gate(s). c1 configuration for idle qubit effects along with best configurations, namely c14 for LA and c12 for SA, and the worst ones, as c23 for LA and c13 for SA, for parallel gating are shown. b) Same as case a) but for $R_x(-\frac{\pi}{2})$. c) Same as above but for optimized $\sqrt{iSWAP}$ operation(s). c12 configuration is selected to compare the effects on gate infidelity due to idle qubits coupling whereas c12–34 is chosen to show the detrimental action of parallel gating on gate infidelity.

taneous applications of presented gate sequences still appear to be usable in Noisy Intermediate-Scale Quantum (NISQ) applications, *i.e.*, in relatively shallow quantum circuits not equipped with QEC.

We anticipate that lower infidelities for parallel gates could be achieved by searching for configuration-optimized sequences including the simultaneous manipulation of qubits. This approach would entail designing distinct control sequences for different configurations, levels of parallelism, and array types. The exploration of optimized gate sequences for arbitrary arrays will be part of our future work.

4. Conclusion

We have simulated LA and SA of four FF qubits affected by electric noise including interactions with idling qubits and driven by simultaneous gating to study their effects on the entanglement gate fidelity.

The analysis of the results on the LA revealed that configurations with the manipulated qubit positioned on an array edges experienced lower infidelity, attributed to the reduced number of neighboring idle qubits. The $\sqrt{iSWAP}$ gate showed poor robustness to electrical noise and exhibited higher infidelity, especially when operating on qubits in the middle of the array. This difference vanishes when optimized sequences for the $\sqrt{iSWAP}$ gate

are exploited. Parallel gating effects showcased the importance of which qubits are simultaneously manipulated, with qubit configurations closer to the array edges generally exhibiting lower gate infidelities.

Shifting the focus to the SA, simulation results revealed that gate fidelity degradation induced by idle qubits was more pronounced than in the LAParallel gating showed increased inter-qubit coupling with idle qubits, resulting in higher infidelity, especially evident for $\sqrt{iSWAP}$ gates.

Upon comparing the fidelity results between the two array types, we consistently observed higher infidelity in the SA for each considered configuration. This can be attributed to the denser qubit packing of the SA, which results in increased inter-qubit couplings leading to unwanted interactions.

5. Experimental Section

The entanglement fidelity F[18–20] was a figure of merit that did not depend on the initial condition chosen for the qubit and is given by

$$F = tr[\rho^{RS}\mathbb{1}_R \otimes (U_i^{-1}U_d)_S \rho^{RS}\mathbb{1}_R \otimes (U_d^{-1}U_i)_S] \tag{11}$$

where U_i (U_d) is the ideal (disturbed) quantum gate and $\rho^{RS} = |\psi\rangle\langle\psi|$, where $|\psi\rangle = \frac{1}{\sqrt{2}}(|0\rangle^{\otimes 2n} + |1\rangle^{\otimes 2n})$ for a n-qubit gate, with n = 1, 2, and 4, represents a maximally entangled state in a double state space generated by two identical Hilbert spaces R and S.

**ADVANCED
SCIENCE NEWS**

www.advancedsciencenews.com

**ADVANCED
QUANTUM
TECHNOLOGIES**

www.advquantumtech.com

In the disturbed quantum gate U_d the 1/f noise model was included. In this model the power spectral density was inversely proportional to the frequency and was given by $S(\omega) = \alpha_{\Delta E_z}/(\omega t_0)$, where $\alpha_{\Delta E_z}$ was the noise amplitude, that did not depend on ω, and t_0 was the time unit. As done in ref. [21], the 1/f noise in the frequency domain was generated as $n(\omega) = m(\omega)^{-1/2}e^{i\varphi(\omega)}$, where $m(\omega)$ was generated from a standard Gaussian white process and $\varphi(\omega) = [0, 2\pi]$ was a phase factor chosen uniformly. Then, the inverse Fourier transform was calculated and the result was multiplied by $\alpha_{\Delta E_z}$ to obtain the noise in the time domain.

For each gate under study, 100 instances of the 1/f charge noise were generated in the time domain and added to the ideal sequence signals generating the operation for each qubit. Finally, an average of the resulting entanglement infidelities was performed.

Conflict of Interest

The authors declare no conflict of interest.

Data Availability Statement

The data that support the findings of this study are available from the corresponding author upon reasonable request.

[1] A. Morello, J. J. Pla, P. Bertet, D. N. Jamieson, *Adv. Quantum Technol.* **2020**, *3*, 2000005.

[2] A. Chatterjee, P. Stevenson, S. D. Franceschi, A. Morello, N. de Leon, F. Kuemmeth, *Nat. Rev. Phys.* **2021**, *3*, 157.

[3] G. Burkard, T. D. Ladd, A. Pan, J. M. Nichol, J. R. Petta, *Rev. Mod. Phys.* **2023**, *95*, 025003.

[4] M. De Michielis, E. Ferraro, E. Prati, L. Hutin, B. Bertrand, E. Charbon, D. J. Ibberson, M. F. Gonzalez-Zalba, *J. Phys. D: Appl. Phys.* **2023**, *56*, 363001.

[5] G. Tosi, F. A. Mohiyaddin, V. Schmitt, S. Tenberg, R. Rahman, G. Klimeck, A. Morello, *Nat. Commun.* **2017**, *8*, 450.

[6] G. Tosi, F. A. Mohiyaddin, S. Tenberg, A. Laucht, A. Morello, *Phys. Rev. B* **2018**, *98*, 075313.

[7] D. Rei, E. Ferraro, M. De Michielis, *Adv. Quantum Technol.* **2022**, *5*, 2100133.

[8] E. Ferraro, D. Rei, M. Paris, M. De Michielis, *EPJ Quantum Technol.* **2022**, *9*, 2.

[9] F. A. Calderon-Vargas, E. Barnes, S. E. Economou, *Phys. Rev. B* **2022**, *106*, 165302.

[10] R. Savytskyy, T. Botzem, I. F. de Fuentes, B. Joecker, J. J. Pla, F. E. Hudson, K. M. Itoh, A. M. Jakob, B. C. Johnson, D. N. Jamieson, A. S. Dzurak, A. Morello, *Sci. Adv.* **2023**, *9*, eadd9408.

[11] D. Zajac, T. Hazard, X. Mi, E. Nielsen, J. R. Petta, *Phys. Rev. Appl.* **2016**, *6*, 054013.

[12] D. Rotta, M. De Michielis, E. Ferraro, M. Fanciulli, E. Prati, *Quantum Inf. Proc. Top. Coll.* **2016**, *15*, 2253.

[13] A. G. Fowler, C. D. Hill, L. C. L. Hollenberg, *Phys. Rev. A* **2004**, *69*, 4.

[14] Y. Li, S. C. Benjamin, *npj Quantum Inf.* **2018**, *4*, 1.

[15] O. Crawford, J. R. Cruise, N. Mertig, M. F. Gonzalez-Zalba, *npj Quantum Inf.* **2023**, *9*, 13.

[16] A. Kitaev, *Ann. Phys.* **2003**, *303*, 2.

[17] A. G. Fowler, M. Mariantoni, J. M. Martinis, A. N. Cleland, *Phys. Rev. A* **2012**, *86*, 032324.

[18] S. Mehl, *Phys. Rev. B* **2015**, *91*, 035430.

[19] B. Schumacher, *Phys. Rev. A* **1996**, *54*, 2614.

[20] M. A. Nielsen, arXiv:quant-ph/9606012 **1996**.

[21] E. Ferraro, M. De Michielis, *Sci. Rep.* **2020**, *10*, 17780.